CrossMark

Faculae Cancel out on the Surfaces of Active Suns

N.-E. Nèmec[1,2] , A. I. Shapiro[2] , E. Işık[3] , K. Sowmya[2] , S. K. Solanki[2,4] , N. A. Krivova[2] , R. H. Cameron[2] , and L. Gizon[1,2,5]
[1] Institut für Astrophysik und Geophysik, Georg-August-Universität Göttingen, Friedrich-Hund-Platz 1, D-37077 Göttingen, Germany;
nina-elisabeth.nemec@uni-goettingen.de
[2] Max-Planck-Institut für Sonnensystemforschung, Justus-von-Liebig-Weg 3, D-37077 Göttingen, Germany
[3] Department of Computer Science, Turkish-German University, Şahinkaya Cd. 94, Beykoz, 34820 Istanbul, Turkey
[4] School of Space Research, Kyung Hee University, Yongin, Gyeonggi 446–701, Republic of Korea
[5] Center for Space Science, NYUAD Institute, New York University Abu Dhabi, Abu Dhabi, UAE

Abstract

Surfaces of the Sun and other cool stars are filled with magnetic fields, which are either seen as dark compact spots or more diffuse bright structures like faculae. Both hamper detection and characterization of exoplanets, affecting stellar brightness and spectra, as well as transmission spectra. However, the expected facular and spot signals in stellar data are quite different, for instance, they have distinct temporal and spectral profiles. Consequently, corrections of stellar data for magnetic activity can greatly benefit from the insight on whether the stellar signal is dominated by spots or faculae. Here, we utilize a surface flux transport model to show that more effective cancellation of diffuse magnetic flux associated with faculae leads to spot area coverages increasing faster with stellar magnetic activity than that by faculae. Our calculations explain the observed dependence between solar spot and facular area coverages and allow its extension to stars that are more active than the Sun. This extension enables anticipating the properties of stellar signal and its more reliable mitigation, leading to a more accurate characterization of exoplanets and their atmospheres.

Unified Astronomy Thesaurus concepts: Stellar astronomy (1583); Solar physics (1476)

Supporting material: animation

1. Introduction

The magnetic fields emerging on solar and stellar surfaces lead to the formation of surface magnetic features, such as dark spots and bright faculae (see, e.g., Solanki et al. 2006 for a review of the solar case). An exciting manifestation of these magnetic features is the temporal variation of brightness of the Sun and solar-like stars (Solanki et al. 2013; Ermolli et al. 2013; Kopp & Shapiro 2021).

The most precise records of solar brightness are obtained by spaceborne radiometers that measure the total solar irradiance (TSI), i.e., the wavelength-integrated solar radiative flux normalized to a distance of 1 au (see Kopp 2014 for review). These measurements of the TSI revealed that it varies along the course of the 11 yr sunspot activity cycle. Namely, the TSI is about 0.1% higher at the solar maximum than at the solar minimum. This implies that the decrease of the TSI due to spots is overcompensated by the increase caused by faculae, i.e., the TSI variability on the activity cycle timescale is facula dominated (see, e.g., the detailed discussion and references in Shapiro et al. 2016).

Concurrently to solar studies, a significant effort was invested in studying magnetic activity cycles and brightness variations of other stars. Long-term monitoring programs of stellar variability began in the 1960s, as Olin Wilson established the Mount Wilson observations of the Ca II H and K lines. The emission in Ca II H and K lines formed in stellar chromosphere is a good proxy of magnetic heating, so
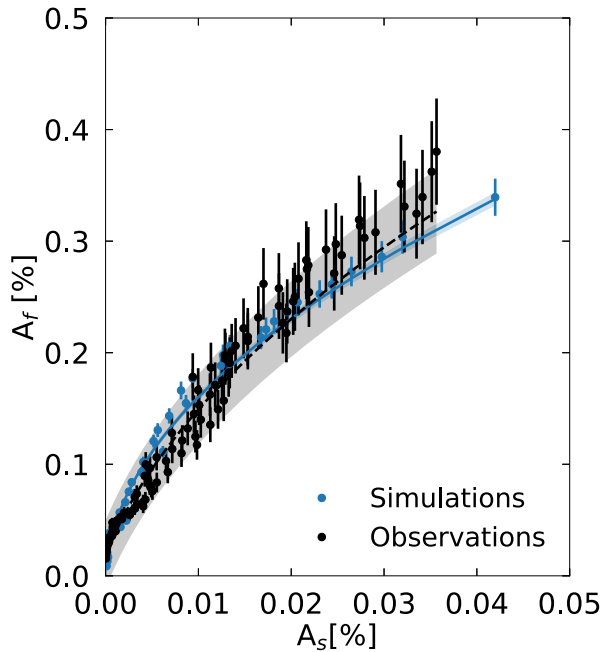
that the Mount Wilson program allowed studying variations of stellar magnetic activity. The next big step in observations of stellar variability became the establishment of the Lowell Observatory monitoring program (Lockwood et al. 1992). This program conducted observations in the visual spectral domain in the Strömgren b and y filters, which are centered at wavelengths of 467 and 547 nm, respectively. Simultaneous measurements of stellar photometric brightness and chromospheric activity revealed a distinction between active young and less active old stars (e.g., Lockwood et al. 1997; Radick et al. 1998, 2018; Lockwood et al. 2007). It turned out that the Ca II line emission and the Strömgren b and y brightness are positively correlated (i.e., the increase in the Ca II emission is accompanied by an increase in the photometric brightness, like for the Sun) for less active stars and negatively correlated in more active stars.

Shapiro et al. (2014) showed that this transition from faculae- to spot-dominated stellar brightness variability can be explained by a simple extrapolation of solar observation that faculae-to-spot area ratio decreases with increasing activity level (Foukal 1993; Chapman et al. 1997; Foukal 1998). An intriguing application of this result is that it provides evidence that the relation between facular and spot disk coverages observed on the Sun is valid, at least qualitatively, also for other solar-like stars and, in particular, for stars more active than the Sun. This raises the question about the physical mechanism behind this relation.

In this study we employ the surface flux transport model (in the form of Işık et al. 2018) to model the emergence and evolution of flux on the surfaces of stars. Then we obtain the area coverage of faculae and spots following the approach presented in Nèmec et al. (2020, hereafter N20). In

Figure 1. The dependence of the facular area coverage on that of spots as returned by our forward model (blue) and retrieved from solar observations (black). Dots represent 58 day binned values (see the text); the vertical lines represent the standard deviations in the corresponding bins. The solid curves represent least-squares fits with the function $A_f = a \cdot \sqrt{A_s + c} + d$, and shaded areas are the 1σ uncertainties of the fits.

Sections 2.1 and 2.2. we demonstrate that our model allows reproducing both solar and stellar data. In Section 3 we then use our model to explain what leads to the decrease of the faculae-to-spot ratio with magnetic activity.

2. Facular and Spot Disk Coverages: Model versus Observations

2.1. The Sun

We first considered a single cycle on a star with the activity level corresponding to solar cycle 22 (1986–1996). For this we applied a record of active-region emergences in the form of bipolar magnetic regions (BMRs) calculated from a semiempirical model of the solar cycle (Jiang et al. 2011a) and ran the SFTM to obtain daily surface distributions of magnetic field. A detailed description of the SFTM setup is given in Appendix A.

We then followed the approach developed in N20 to transform these distributions to maps of visible disk distribution of faculae and spots. In Figure 1 we plot the forward-modeled relation between the disk area coverage of faculae, A_f, and that of spots, A_s, for a star with activity level corresponding to solar cycle 22 and compare it to solar observations collected by Shapiro et al. (2014). The daily values of A_f and A_s were both sorted according to ascending A_s, before binning them in 58 day intervals to remove the effect of solar rotation. This interval is the same as in Shapiro et al. (2014) and ensures that effects that are purely due to transits of features (i.e., due to the solar rotation) are removed. Longer intervals than several solar rotations would on the other hand remove the effects of the evolution of the magnetic features, which are of interest in the present work. We have checked that the result it not affected by reasonable choices of binning intervals (i.e., over one or three solar rotations). Figure 1 demonstrates that our calculations

reproduce the observed trend of facular area increasing less rapidly with magnetic activity than the spot area.
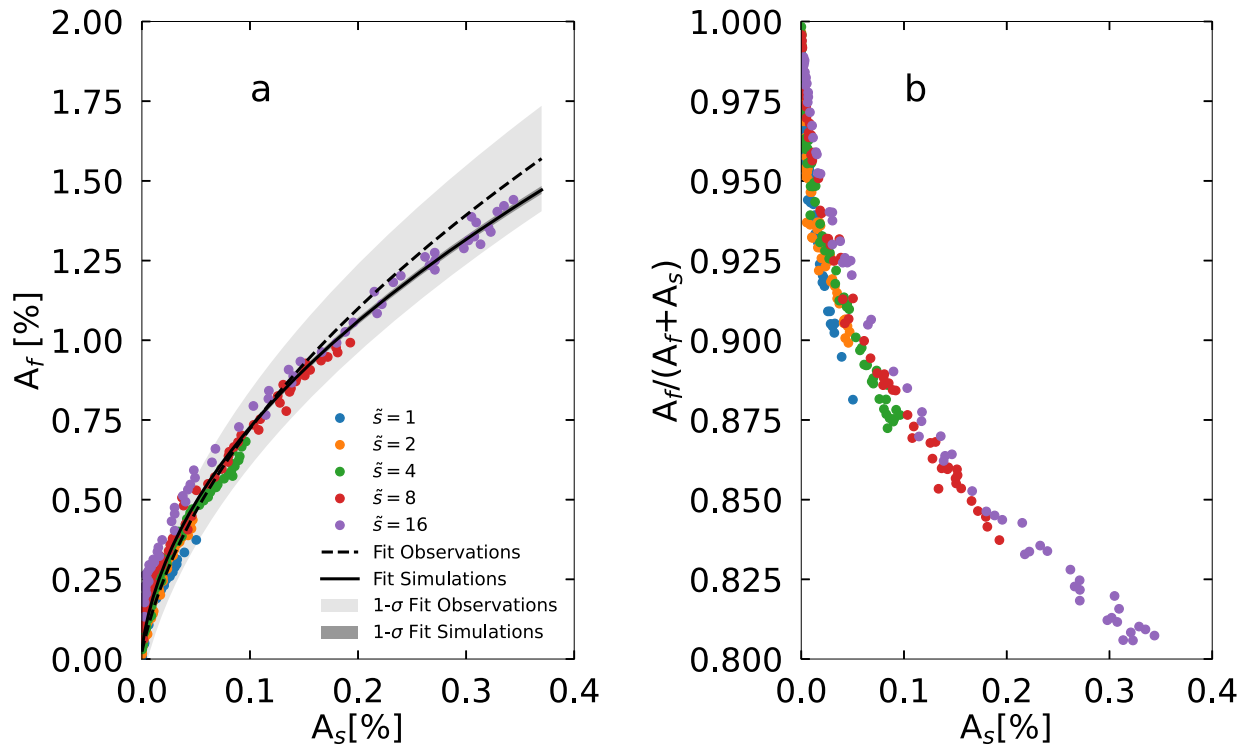
2.2. Active Stars

We now extend the model to stars more active than the Sun before unveiling the physical mechanisms responsible for this curious behavior of facular and spot coverages. We model active stars by filling their surfaces with gradually increasing amounts of magnetic flux. This is achieved by scaling the number of emergences by a given factor, $\tilde{s}$ (see Işık et al. 2018 and Appendix B), and running the SFTM model again. A star with, for example, $\tilde{s} = 2$ experiences twice as many emergences than the solar case $\tilde{s} = 1$.

The resulting facular and spot areas are shown Figure 2(a), where we plot together calculations representing the Sun during cycle 22 ($\tilde{s} = 1$), more active stars ($\tilde{s} = 2, 4, 8, 16$; see Appendix B), and the fits to the solar area coverages from Figure 1, which were extrapolated toward higher spot areas. Figure 2(b) additionally gives the ratio of facular area coverage to total area coverage by magnetic features (i.e., the sum of faculae and spots) to detail the decrease in the facular component of magnetic activity. All in all, Figures 2(a) and (b) indicate that the decrease of the facular-to-spot ratio with activity continues also well beyond the observed level of solar activity.

While comparing our results to solar data was relatively straightforward, only some indirect measurements of spot coverages of solar-like stars are available, and there is basically no reliable technique for measuring facular coverages. Thus, we cannot directly test the dependencies plotted in Figure 2 against stellar observations. Instead we opted to investigate whether the modeled trends in disk coverages by magnetic features are consistent with the observed variability of stellar brightness along the course of stellar activity cycles. In particular, synoptic programs at the Lowell and Fairborn observatories (Lockwood et al. 1992, 2007; Radick et al. 1998, 2018) revealed that an increase of stellar activity (quantified via the S-index, which is a measure of stellar emission in the Ca II H and K lines and is routinely used as a proxy of stellar magnetic activity) in time is accompanied by an increase in the stellar photometric brightness in Strömgren (b +y)/2 for stars with similar activity levels as that of the Sun. However, stars with higher activity levels show an anticorrelation between magnetic activity and photometric brightness (i.e., the star gets photometrically darker with increasing Ca II H and K emission).

Previous studies indicated that such a transition can be reproduced by extrapolating the observed dependencies of solar facular and spot area coverage on the S-index (Shapiro et al. 2014). Instead of relying on these extrapolations, which are purely empirical and assume that any trend seen on the Sun continues unchanged to more active stars, we combined our calculations of spot and facular coverages with models of stellar photometric brightness from N20 and Ca II H and K emission developed by Sowmya et al. (2021). Namely, we used the model introduced in N20 to calculate the activity-induced alteration in Strömgren (b+y)/2, $(b + y)/2_{\text{quiet}} - (b + y)/2_{\text{active}}$, where the first term represents the brightness of a star free from any magnetic features and the second term quantifies the brightness in the presence of magnetic activity (so that a positive alteration of Strömgren (b +y)/2 corresponds to an overall brightening with increasing

Figure 2. Similar to Figure 1, but the forward-modeled dependence is plotted for stars with different levels of magnetic activity. Panel (b) gives the fraction of faculae in total area of active regions as a function of the spot area.

magnetic activity, while a negative alteration corresponds to a dimming). These calculations have been performed for the daily snapshots of the disk distributions of magnetic features for all activity levels ($\tilde{s}$) used in this study (see Figures 1(b) and (c)). Then we used the Sowmya et al. (2021) model for the Ca II H and K emission to calculate the corresponding S-index values. As a result, we obtained a contemporaneous time series of Strömgren $(b+y)/2$ and the S-index, by combining all five modeled activity levels into a 55 year time series. We then sorted both time series according to ascending S-index values, before calculating values averaged over bins containing 365 sorted data points shown in Figure 3. One can see that the alteration in Strömgren $(b+y)/2$ varies with the S-index, following a second-degree polynomial, and changing its sign at an S-index value of about 0.195, which is only slightly above the maximum of 0.188 observed on the Sun (Shapiro et al. 2014).

Similar to the measurements from the Lowell and Fairborn programs, we calculated the slope between the changes of stellar photometric brightness and the S-index over the course of the magnetic activity cycle, $\Delta[(b+y)/2]/\Delta S$. In this metric, positive values correspond to facula-dominated photometric variability as observed on the Sun and inactive stars. Negative values conversely correspond to spot-dominated photometric variability as observed on active stars. In Appendix C we show how to transform the dependence plotted in Figure 3 into the dependence of $\Delta[(b+y)/2]/\Delta S$ on the stellar activity level. Figure 4 presents the comparison of our model output. As stars are observed from various, mostly unknown inclination angles i (i.e., angles between the direction to the observer and the stellar rotation axis), we show the calculations performed for two extreme cases: $i = 90°$ (i.e., stars observed equator-on) and $i = 0°$ (i.e., stars observed pole-on) in comparison to the Lowell and Fairborn data (Radick et al. 2018). We note that the

inclination affects the variability by changing the disk distribution of magnetic features. For example, on stars like the Sun the magnetic features are mainly concentrated in the near-equatorial bands so that the change of the inclination from $i = 90°$ to $i = 0°$ will shift the magnetic features toward the (visible) limb, affecting both photometric variability (see Nèmec et al. 2020) and the S-index (see Sowmya et al. 2021). In Figure 4 we show stars with values of effective temperatures ±200 K around the solar effective temperature. Such a choice is motivated by the strong dependence of facular and spot brightness contrast (and, thus, the regime of the variability) on stellar effective temperature (see, e.g., Witzke et al. 2018, 2020; Panja et al. 2020).

Our calculations agree well with observations, especially for stars with near-solar values of effective temperature. In particular, our model explains the observed transition between faculae- and spot-dominated variability and highlights the importance of the inclination angle for solar–stellar comparisons. We construe this as a confirmation that our model properly reproduces the relation between spot and facular coverages not only for the Sun but also for more active stars.

3. Discussion and Conclusions

All in all, the ability of our model to reproduce both solar and stellar data allows discussing a physical mechanism in charge of the decrease of the faculae-to-spot ratio with magnetic activity. The instantaneous ratio (i.e., observed at a given time) between facular and spot area coverages depends on (a) the ratio between those parts of a newly emerged BMR attributed to faculae and spots ("driver ratio"), as well as on (b) the decay rates of faculae and spots. The size distribution of the BMRs in our model is fixed (with a slight dependence on the cycle phase; Işik et al. 2018). With increasing activity level (
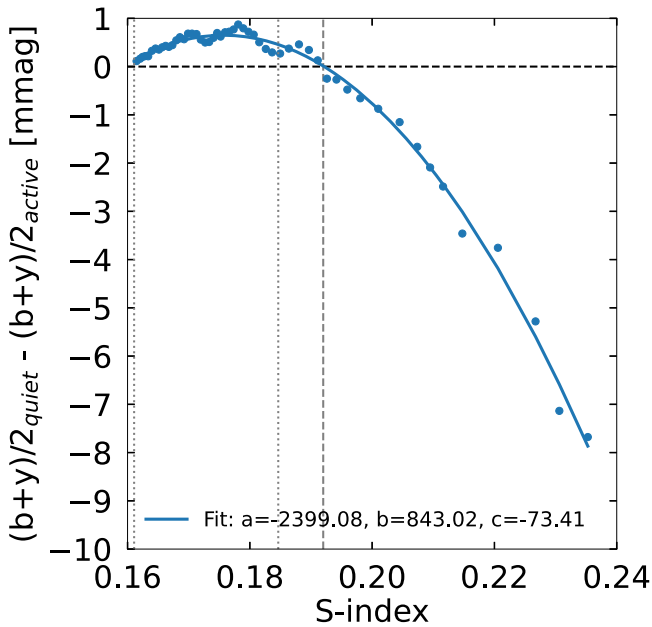
Figure 3. Magnetic alteration of stellar brightness in Strömgren $(b+y)/2$ as a function of S-index. Plotted are 365 day binned values (blue dots; see the text) and standard deviations of brightness within each of the bins (vertical blue bars, which are mostly smaller than the dot size). The solid blue line gives the fit of the second-degree polynomial in the form of $aS^2 + bS + c$, with the coefficients of the fit shown in the legend. The horizontal black dashed line indicates the zero level, and the vertical gray dashed line points to the S-index value, at which the transition from faculae-to-spot magnetic alteration occurs. Vertical dotted gray lines indicated the minimum and maximum value of the calculations representing the Sun.
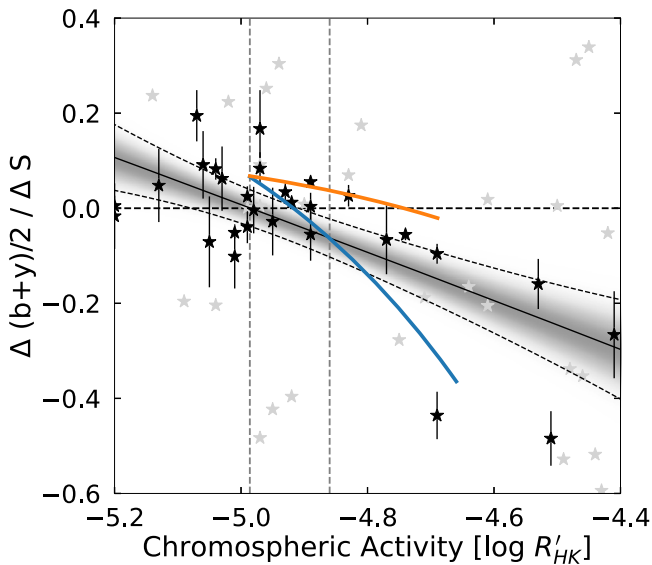
Figure 4. $\Delta[(b+y)/2]/\Delta S$ plotted against the mean chromospheric activity expressed through $\log R'_{HK}$. The blue and orange solid lines represent the modeled dependencies for $i = 90°$ and $i = 0°$, respectively, while asterisks show the Lowell and Fairborn measurements (Radick et al. 2018). Black asterisks indicate stars with effective temperatures ±200 K around the solar value (5777 K) and with uncertainty in $\Delta[(b + y)/2]/\Delta S$ (as indicated by the black bars) below 0.1. Gray asterisks depict the rest of the Lowell and Fairborn sample. The dashed horizontal line indicates the zero level, where the transition between faculae-to-spot dominated occurs, and the two vertical gray dashed lines indicate the minimum and maximum values of solar activity during cycle 22. The gray-shaded band shows the result of the Bayesian linear regression to the black asterisks using Gaussian priors for the parameters of a quadratic polynomial. The solid curve shows the maximum of the posteriori estimate and the shaded region represents the probability density of the posterior distribution. The dashed curves denote the 2σ posterior boundaries.

i.e., higher BMR emergence frequency) this distribution is still preserved (see Appendix B), which means that the driver ratio in our model is assumed to be independent on the activity level. The spots decay linearly in time, while the decay rate remains the same for all spots, such that the Gnevyshev–Waldmeier relation (Waldmeier 1955) between sunspot sizes and lifetimes is satisfied. The area coverage by faculae is generally larger than those of spots (see Figures 1 and 2). This in turn means that cancellation of fluxes of opposite polarities, both directly upon emergence and during the subsequent evolution of surface flux are more likely. As the activity level increases, opposite-polarity facular flux elements lie close to each other more frequently. This leads to more efficient flux cancellation, resulting in shortening of the facular lifetime. Consequently, a more efficient cancellation of the magnetic flux at higher activity levels leads to the drop of the ratio between facular and spot area coverages (see Appendix D for a simple illustrative experiment). We note that our model also takes into account the cancellation of spots with different polarities. However, since the spot areas are much smaller than those of faculae and their lifetimes are much shorter, such cancellations barely occur.

In our numerical experiments, we assumed that active stars simply display higher amounts of flux emergence than the present Sun. At the same time, more active stars are often younger and rotate faster (although there is a significant scatter in the activity–rotation period dependency; e.g., see Barnes 2007). Here we neglect this trend and the associated modification of the surface distribution of the magnetic region emergence (Işık et al. 2018). We, thus, focused purely on the increasing probability of superposition of emerging and evolving surface flux elements to isolate this effect. We note that the good agreement between our calculations and solar/ stellar data by no means excludes the effect of rotation on magnetic emergences, but merely shows that the cancellation mechanism suggested in the present work plays a decisive role in determining the ratio between facular and spot coverages.

Our study shows that while facular contribution to stellar signals decreases with stellar activity, faculae play a significant role in magnetically driven signals of low activity stars. This is of particular importance to planet-hosting low activity stars since radial velocity monitoring and transmission spectroscopy observations aimed at characterizing planets and their atmospheres, respectively, choose such stars as their main targets.

Appendix A

The SFTM describes the passive transport of the radial component of the magnetic field B, considering the effects of differential rotation $\Omega(\lambda)$ (with λ being the latitude), meridional flow $\nu(\lambda)$ at the solar surface, and a horizontal surface diffusion thanks to a nonzero horizontal diffusivity η_H (50 km^2 s^{-1} taken from Cameron et al. 2010). The emerged active regions gradually disperse due to the radial diffusion η_r (25 km^2 s^{-1} as set by Jiang et al. 2011b), with the flux finally decaying after cancellation between opposite polarities, where they overlap.
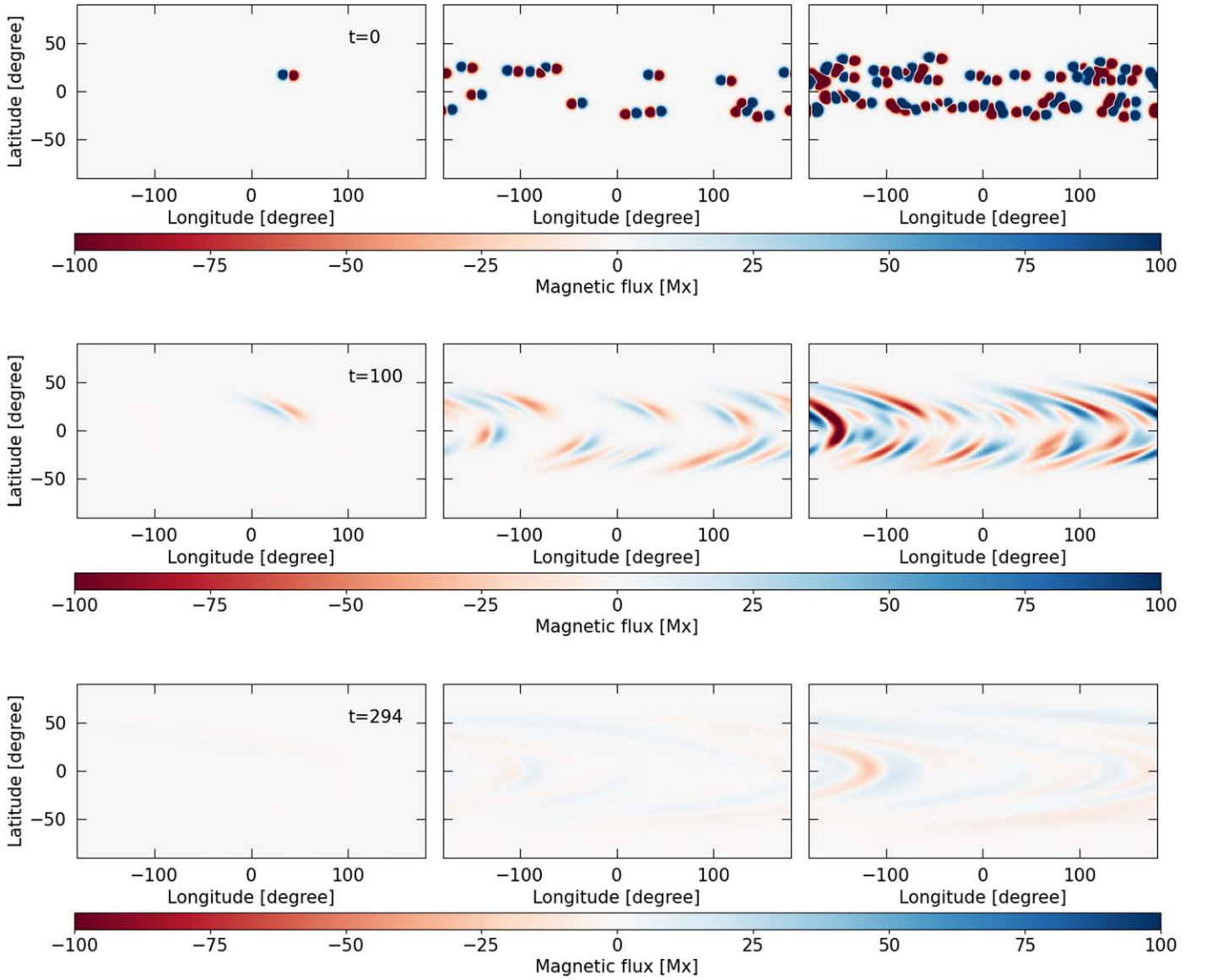
Figure 5. Distribution of the magnetic flux associated with faculae in the simple simulation setup. Shown are simulations for the $\tilde{s} = 1$ (left column), $\tilde{s} = 16$ (middle column), and $\tilde{s} = 64$ (right column); rows correspond to different timestamps in the available animation. The animation shows the decay of flux from the time of emergence until 295 days after. The duration of the animation is 17 s.

(An animation of this figure is available.)

The governing equation is

$$
\frac{\partial B}{\partial t} = -\Omega(\lambda)\frac{\partial B}{\partial \phi} - \frac{1}{R_\odot \cos\lambda}\frac{\partial}{\partial \lambda}(\nu(\lambda)B\cos(\lambda))
$$
$$
+ \eta_H\left(\frac{1}{R_\odot^2 \cos\lambda}\frac{\partial}{\partial \lambda}\left(\cos(\lambda)\frac{\partial B}{\partial \lambda}\right) + \frac{1}{R_\odot^2 \cos^2\lambda}\frac{\partial^2 B}{\partial \phi^2}\right)
$$
$$
+ D(\eta_r) + S(\lambda, \phi, t),
$$

$$(A1)$$

where $R_\odot$ is the solar radius, ϕ is the longitude of the active region, and D is a linear operator that describes the decay due to radial diffusion with the radial surface diffusivity η_r (Baumann et al. 2006). The time-averaged (synodic) differential rotation profile was taken from Snodgrass (1983) and the time-averaged meridional flow is expressed following van Ballegooijen et al. (1998). The magnetic flux in the model is injected as bipolar magnetic regions (BMRs, with one BMR consisting of two neighboring flux concentrations with opposite polarities). The emergence of the BMRs is introduced via the source term that determines the position and time of the emerging flux, as well as the flux density of each polarity patch, namely,

$$
B^\pm(\lambda, \phi) = B_{\max}\left(\frac{0.4\Delta\beta}{\delta}\right)^2 e^{(-2[1-\cos(\beta_\pm(\lambda,\phi))]/\delta^2)}, \quad (A2)
$$

where $\beta_\pm(\lambda,\phi)$ is the heliocentric angle between a given point with latitude and longitude (λ, ϕ) and the centers of the polarity patches, $\Delta\beta$ is the angular separation between the centers of the two polarities, and δ is the size of the individual polarity patch, taken to be $4°$. $B_{\max}$ is a scaling factor set to 374 G (Cameron et al. 2010; Jiang et al. 2011b). The source term is compiled following the procedure described in Cameron et al. (2010)
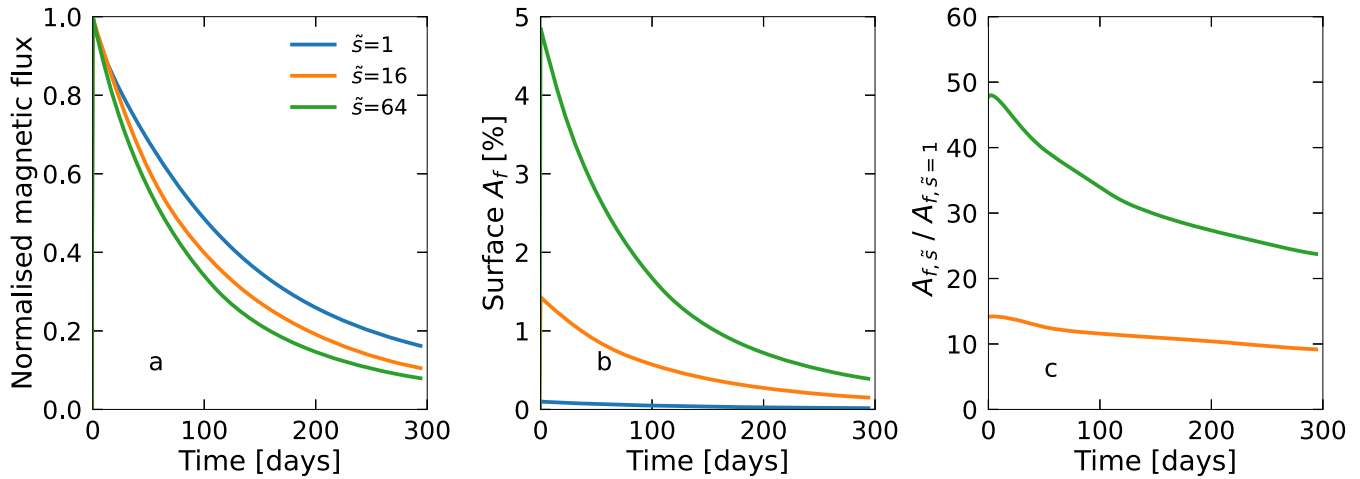
Figure 6. Demonstration of the effect of flux cancellation on the magnetic field and facular area coverages. Shown are calculations with 1 ($\tilde{s} = 1$, blue), 16 ($\tilde{s} = 16$, orange), and 64 ($\tilde{s} = 64$, orange) active regions. Panel (a) shows the evolution of the surface magnetic flux normalized to corresponding value at the moment of emergence ($t = 0$). Panel (b) shows the surface area coverage by faculae in percent. Panel (c) shows the ratios of facular coverages for $\tilde{s} = 16$ and $\tilde{s} = 64$ cases to that for $\tilde{s} = 1$ case (orange and green curves, respectively). Calculations are based on the magnetograms shown in Figure 5.

with the statistics of solar BMR emergences from Jiang et al. (2011b). All in all, the source term represents, statistically, the observed distribution of tilt angles, sizes, emergence frequency, and emergence latitudes of solar cycle 22, with the longitudes being randomized.

When converting the magnetic flux of the SFTM output from Işık et al. (2018), three free parameters from N20 are used: the linear decay rate of the spots R_d, the linear growth rate of the spots R_g, and the faculae saturation threshold $B_{\rm sat}$ as defined in Krivova et al. (2003). As the input record in the present approach is different, we adjusted the free parameters to reproduce the area coverages of N20. This resulted in values of $R_g = 600$ MSH/day , $R_d = 47$ MSH/day and $B_{\rm sat} = 470$ G.

Appendix B

We define the time-dependent emergence rate of BMRs on a star $S_\star$ as $S_\star(t) = S_\odot(t) \cdot \tilde{s}$, where $S_\odot(t)$ is the time-dependent solar BMR emergence rate of solar cycle 22 and $\tilde{s}$ is a scaling factor, following the notation in Işık et al. (2018). This means that a star with $\tilde{s} = 2$ exhibits 2 times more BMR emergences compared to the solar case, $\tilde{s} = 1$. As noted by Jiang et al. (2011a) and taken into account by Işık et al. (2018), there is a weak linear dependence of the mean latitude of BMR emergence on the cycle amplitude (e.g., the cycle-integrated number of emergences). We took this relationship into account when modeling a more active solar cycle. At the same time the size distribution of the BMRs of $\tilde{s} = 1$ is preserved also for stars with higher BMR emergence frequency. We neglect effects of the rotation on the latitude of emergence in this work. Similar to considering different inclination angles, shifting the activity belt of active-region emergence toward higher latitudes will result in different visible disk areas due to foreshortening and will affect the intensity contrasts of the magnetic features (see Shapiro et al. 2014; Işık et al. 2018).

Appendix C

Monitoring of stellar Ca II H and K emission revealed that the amplitude of the stellar activity cycle in the S-index is proportional to the cycle-averaged value of the S-index (Hall et al. 2009). We use this property to generate an S-index time series of active stars (i.e., stronger cycles) by linearly scaling the annual averages of the solar S-index for cycle 22. For each S-index, we obtained a time series of the annual S-index (Shapiro et al. 2014, 2020). Then we used the polynomial fit from Figure 3 to generate a corresponding photometric time series and applied linear regression for the variability in Strömgren (b+y)/2 as a function of the annually averaged S-index, to calculate the slope parameter $\Delta[(b+y)/2]/\Delta S$. We note that while the scaling of the solar S-index using the activity cycle employed here is only an approximation, we do not expect it to have a major effect on our calculations of the regression coefficient.

Appendix D

Here we present a simple experiment, which demonstrates the effect of flux cancellation. We prescribe all emerging active regions to have a size of $\Delta\beta = 10°$, representing the largest regions in our input record and perform the calculations for $\tilde{s} = 1$, 16, and 64, with all BMRs emerging at the same moment of time $t = 0$.
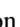
In Figure 5 we show the snapshots from the animation illustrating the evolution of magnetic flux for all three cases considered here. One can see that the cancellation of magnetic flux from different active regions happens both during the emergence (see overlapping active regions in the top middle and left panels) as well as during the subsequent evolution.

Figure 6 shows the time evolution of the magnetic flux (panel (a)), the facular area coverages (panel (b)), and the ratio of facular area coverages for $\tilde{s} = 16$ and 64 cases to that for $\tilde{s} = 1$ case (panel (c)). One can see that both the magnetic flux and facular area coverages decrease nonlinearly with time. Furthermore, the flux drops faster for higher values of $\tilde{s}$ (see Figure 6(a)). This implies that the flux cancellation gets stronger with the increase of the emergence rate and magnetic activity.

We note that the flux cancellation happens not only during the evolution of active regions but also directly at the moment of emergence. Indeed, $A_{f,\tilde{s}=16}/A_{f,\tilde{s}=1}$ at $t = 0$ is about 14,

while the corresponding $A_{f,\bar{s}=64}/A_{f,\bar{s}=1}$ is about 50 (see the intersection of orange and green curves with the ordinate $t=0$ in Figure 6(c)). Both these values are below the scaling factor for the emergence rate (16 and 64, respectively) so that the surface flux increases slower than the emergence rate, implying a cancellation of the magnetic flux at the moment of emergence.

ORCID iDs

N.-E. Nèmec ⓘ https://orcid.org/0000-0001-6090-1247
A. I. Shapiro ⓘ https://orcid.org/0000-0002-8842-5403
E. Işık ⓘ https://orcid.org/0000-0001-6163-0653
K. Sowmya ⓘ https://orcid.org/0000-0002-3243-1230
S. K. Solanki ⓘ https://orcid.org/0000-0002-3418-8449
N. A. Krivova ⓘ https://orcid.org/0000-0002-1377-3067
R. H. Cameron ⓘ https://orcid.org/0000-0001-9474-8447
L. Gizon ⓘ https://orcid.org/0000-0001-7696-8665

References

Barnes, S. A. 2007, ApJ, 669, 1167
Baumann, I., Schmitt, D., & Schüssler, M. 2006, A&A, 446, 307
Cameron, R. H., Jiang, J., Schmitt, D., & Schüssler, M. 2010, ApJ, 719, 264
Chapman, G. A., Cookson, A. M., & Dobias, J. J. 1997, ApJ, 482, 541
Ermolli, I., Matthes, K., Dudok de Wit, T., et al. 2013, ACP, 13, 3945
Foukal, P. 1993, SoPh, 148, 219
Foukal, P. 1998, ApJ, 500, 958
Hall, J. C., Henry, G. W., Lockwood, G. W., Skiff, B. A., & Saar, S. H. 2009, AJ, 138, 312
Işik, E., Solanki, S. K., Krivova, N. A., & Shapiro, A. i. 2018, A&A, 620, A177
Jiang, J., Cameron, R. H., Schmitt, D., & Schüssler, M. 2011a, A&A, 528, A82
Jiang, J., Cameron, R. H., Schmitt, D., & Schüssler, M. 2011b, A&A, 528, A83
Kopp, G. 2014, JSWSC, 4, A14
Kopp, G., & Shapiro, A. 2021, SoPh, 296, 60
Krivova, N. A., Solanki, S. K., Fligge, M., & Unruh, Y. C. 2003, A&A, 399, L1
Lockwood, G. W., Skiff, B. A., Baliunas, S. L., & Radick, R. R. 1992, Natur, 360, 653
Lockwood, G. W., Skiff, B. A., Henry, G. W., et al. 2007, ApJS, 171, 260
Lockwood, G. W., Skiff, B. A., & Radick, R. R. 1997, ApJ, 485, 789
Nèmec, N. E., Shapiro, A. I., Krivova, N. A., et al. 2020, A&A, 636, A43
Panja, M., Cameron, R., & Solanki, S. K. 2020, ApJ, 893, 113
Radick, R. R., Lockwood, G. W., Henry, G. W., Hall, J. C., & Pevtsov, A. A. 2018, ApJ, 855, 75
Radick, R. R., Lockwood, G. W., Skiff, B. A., & Baliunas, S. L. 1998, ApJS, 118, 239
Shapiro, A. I., Solanki, S. K., Krivova, N. A., et al. 2014, A&A, 569, A38
Shapiro, A. I., Solanki, S. K., Krivova, N. A., Yeo, K. L., & Schmutz, W. K. 2016, A&A, 589, A46
Shapiro, A. V., Shapiro, A. I., Gizon, L., Krivova, N. A., & Solanki, S. K. 2020, A&A, 636, A83
Snodgrass, H. B. 1983, ApJ, 270, 288
Solanki, S. K., Inhester, B., & Schüssler, M. 2006, RPPh, 69, 563
Solanki, S. K., Krivova, N. A., & Haigh, J. D. 2013, ARA&A, 51, 311
Sowmya, K., Shapiro, A. I., Witzke, V., et al. 2021, ApJ, 914, 21
van Ballegooijen, A. A., Cartledge, N. P., & Priest, E. R. 1998, ApJ, 501, 866
Waldmeier, M. 1955, Ergebnisse und Probleme der Sonnenforschung (2nd ed.; Leipzig: Akademische Verlagsgesellschaft Geest & Portig)
Witzke, V., Reinhold, T., Shapiro, A. I., Krivova, N. A., & Solanki, S. K. 2020, A&A, 634, L9
Witzke, V., Shapiro, A. I., Solanki, S. K., Krivova, N. A., & Schmutz, W. 2018, A&A, 619, A146

Erratum: "Faculae Cancel out on the Surfaces of Active Suns" (2022, ApJL, 934, L23)

N.-E. Nèmec[1,2] , A. I. Shapiro[2] , E. Işık[3] , K. Sowmya[2] , S. K. Solanki[2,4] , N . A. Krivova[2] , R. H. Cameron[2] , and
L. Gizon[1,2,5]

[1] Institut für Astrophysik und Geophysik, Georg-August-Universität Göttingen, Friedrich-Hund-Platz 1, D-37077 Göttingen, Germany
nina-elisabeth.nemec@uni-goettingen.de
[2] Max-Planck-Institut für Sonnensystemforschung, Justus-von-Liebig-Weg 3, D-37077 Göttingen, Germany
[3] Department of Computer Science, Turkish-German University, Şahinkaya Cd. 94, Beykoz, 34820 Istanbul, Turkey
[4] School of Space Research, Kyung Hee University, Yongin, Gyeonggi 446–701, Republic of Korea
[5] Center for Space Science, NYUAD Institute, New York University Abu Dhabi, Abu Dhabi, UAE
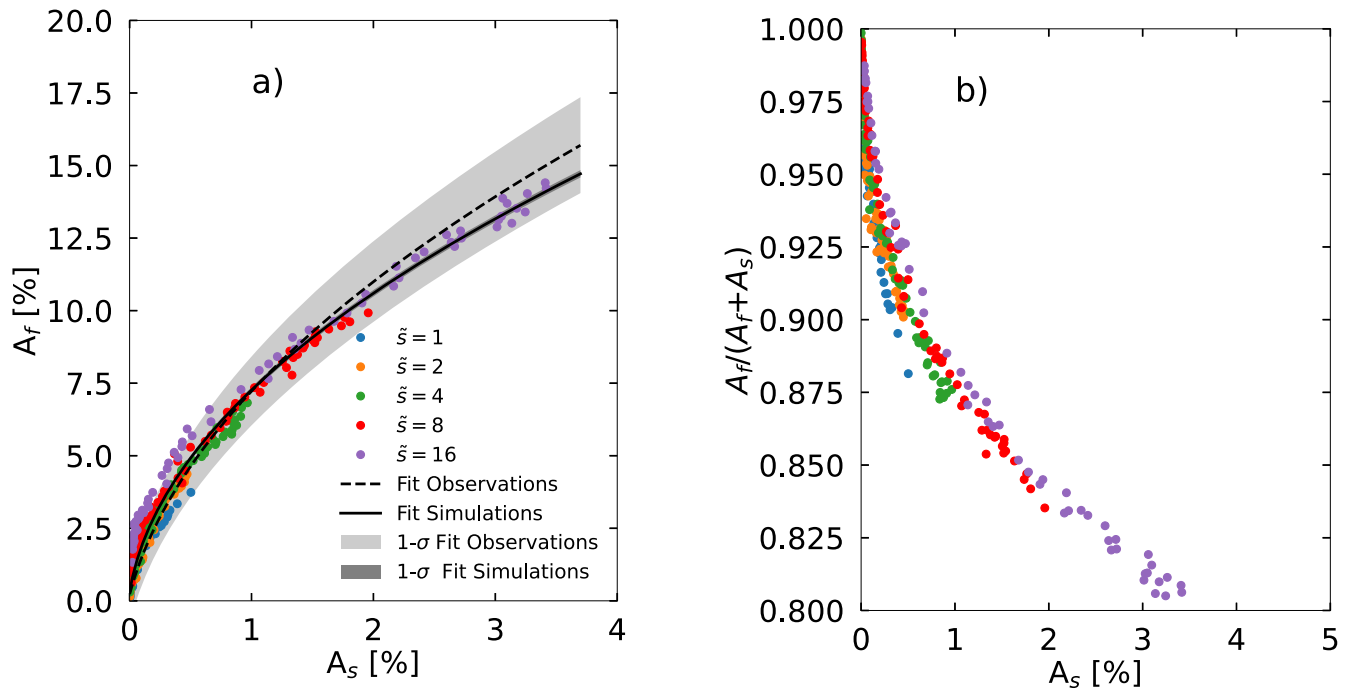Received 2022 August 16; published 2022 September 2

In Figures 1 and 2(a) the values given on the *x*- and *y*-axes, as well as the values on the *x*-axis given in Figure 2(b), do not correspond to the disk area coverage in percent. The values must be multiplied by 10 in order to be in units of percent of the solar/ stellar disk. These plots were solely for demonstration purposes of the change in the area coverages with increasing stellar activity and do not affect the following results and conclusions.
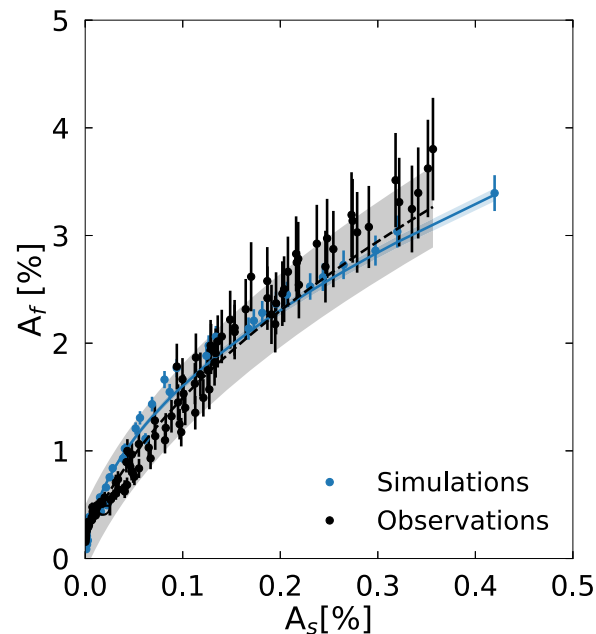
Figure 1. The dependence of the facular area coverage on that of spots as returned by our forward model (blue) and retrieved from solar observations (black). Dots represent 58 day binned values (see the text); the vertical lines represent the standard deviations in the corresponding bins. The solid curves represent least-squares fits with the function $A_f = a \cdot \sqrt{A_s + c} + d$, and shaded areas are the 1σ uncertainties of the fits.

Figure 2. Similar to Figure 1, but the forward-modeled dependence is plotted for stars with different levels of magnetic activity. Panel (b) gives the fraction of faculae in the total area of active regions as a function of the spot area.

ORCID iDs

N.-E. Nèmec ● https://orcid.org/0000-0001-6090-1247
A. I. Shapiro ● https://orcid.org/0000-0002-8842-5403
E. Işık ● https://orcid.org/0000-0001-6163-0653
K. Sowmya ● https://orcid.org/0000-0002-3243-1230

S. K. Solanki ● https://orcid.org/0000-0002-3418-8449
N . A. Krivova ● https://orcid.org/0000-0002-1377-3067
R. H. Cameron ● https://orcid.org/0000-0001-9474-8447
L. Gizon ● https://orcid.org/0000-0001-7696-8665